ARTICLE

Dye-sensitized Er^{3+}-doped CaF_2 nanoparticles for enhanced near-infrared emission at 1530 nm

Received 00th January 20xx,
Accepted 00th January 20xx

DOI: 10.1039/x0xx00000x

Jing Liu,*[a] Min Zeng,[b] Pieter Geiregat,[b] Luca Pilia,[c] Rik Van Deun,[b] and Flavia Artizzu*[b]

Lanthanide (Ln)-doped nanoparticles have shown potential applications in various fields. However, the weak and narrow absorption bands of the Ln ions (Ln^{3+}), hampers efficient optical pumping and severely limits the emission intensity. Dye sensitization is a promising way to boost the near-infrared (NIR) emission of Er^{3+}, hence promoting possible application in optical amplification at 1530 nm, a region that is much sought after for telecommunication technology. Herein, we introduce the fluorescein isothiocyanate (FITC) organic dye with large absorption cross section as energy donor of small-sized (~3.6 nm) Er^{3+}-doped CaF_2 nanoparticles. FITC molecules on the surface of CaF_2 work as antenna to efficiently absorb light, and provide the indirect sensitization of Er^{3+} boosting its emission. In this paper, we employ photoluminescence (PL) and transient absorption (TA) spectroscopy, as well as density functional theory (DFT) calculations to provide and in-depth investigation of the FITC⟶Er^{3+} energy transfer process. The present study proves that an energy transfer efficiency around 92% is achieved in CaF_2:Er^{3+}@FITC nanoparticles resulting in a 28 times enhancement of the Er^{3+} NIR emission. We show that the reason for such a high sensitization efficiency stems from the suitable size and geometry of the FITC dye with a localized transition dipole moment at short distance from the surface of the nanoparticle.

1. Introduction

Due to the unique optical nature of lanthanide ions (Ln^{3+}), characterized by sharp and narrow emission bands and long-lived luminescence, Ln^{3+} based materials have been widely used in amplifiers, lasers, biosensors and so on.[1-6] Ln luminescence can be roughly divided into three types according to different spectral conversion: upconversion, an anti-Stokes process where at least two lower energy photons are converted into a higher energy photon; downconversion, the inverse process of upconversion where a high-energy photon is converted into two low-energy photons; and downshifting, the process where a higher photon is transformed into a lower energy photon.[7,8] This latter phenomenon is of high importance in several technological applications in the near-infrared (NIR) spectral range. In particular, the 1530 nm downshifted luminescence emission of Er^{3+} plays a vital role in information and telecommunication technologies.[9,10] However, currently exploited Er^{3+}-doped fiber amplifiers (EDFAs) present a drawback derived from the narrow and weak absorption cross-section of the Ln^{3+}, resulting in inefficient optical pumping.[11] To improve the absorption, organic dyes working as antennas can be introduced into Er^{3+}-doped materials, owing to the broader absorption spectra and larger absorption cross-sections of dye molecules.[12-14]

Recently, many combinations of dye-sensitized Ln^{3+}-doped upconversion and downconversion nanoparticles have been reported owing to the attainable high emission intensity and the potential interest in photonic and biological applications. The efficiency of the energy transfer (ET) at the organic-inorganic interface in dye sensitized Ln^{3+}-doped nanoparticles has been a central theme in the field in the last years. For instance, Xue and coauthors showed that a detrimental energy back transfer phenomenon is existing in the IR-806 sensitized $NaYF_4$:Yb^{3+},Er^{3+}@$NaYF_4$:Nd^{3+} upconversion nanoparticles.[23] The same authors also pointed out that the optimization of the ratio of the acceptor upconversion nanoparticles to donor dyes is the key to gain efficient dye sensitization. Garfield et al. also reported a dramatic enhancement of the upconversion luminescence intensity and efficiency in comparison with the bare $NaYF_4$:Er^{3+},Yb^{3+} upconversion nanoparticles following the activation of a resonant triplet of dye molecules.[24] Wang and Meijerink[25] postulated dye sensitized Pr^{3+}-Yb^{3+} downconversion luminescence in $NaYF_4$ nanocrystals showing that Förster resonance energy transfer from the coumarin dye to Pr^{3+} leads to around 30 times increase in the Yb^{3+} NIR emission at 980 nm. On the other hand, the research on dye-sensitized downshifted emission is relatively neglected, and to the best of our

[a] Key Laboratory of Luminescence Analysis and Molecular Sensing, Ministry of Education, School of Materials and Energy, Southwest University, Chongqing 400715, P. R. China.
[b] Department of Chemistry, Ghent University, Krijgslaan 281-S3, B-9000, Ghent, Belgium.
[c] Department of Mechanical, Chemical and Material Engineering, University of Cagliari, via Marengo 2, 09123, Cagliari, Italy.
E-mail: jingliu77@swu.edu.cn, flavia.artizzu@ugent.be

†Electronic Supplementary Information (ESI) available: [details of any supplementary information available should be included here]. See DOI: 10.1039/x0xx00000x

knowledge, the study of Er^{3+} NIR downshifting luminescence in dye-sensitized nanoparticles has not been reported up to date. Moreover, the understanding of the ET phenomena at the organic-inorganic interface still needs clarification.

In this work, we present the synthesis, emission properties and a deep investigation of the photocycle of ultra-small (<3.6 nm) Er^{3+}-doped CaF_2 nanoparticles sensitized by fluorescein isothiocyanate (FITC). FITC is a popular dye in biological labeling, because of its high absorptivity, with an extinction coefficient of $\approx 3 \cdot 10^{-16}$ cm^2 at λ_{max} = 500 nm and emission quantum yield.[15,16] It displays visible (Vis) yellow-green light emission and provides pump channels across a spectral region from ultraviolet (UV) to visible (Vis) and it is thus optimal as a sensitizer of Er^{3+}-doped fluoride nanoparticles to boost the near infrared (NIR) emission.[16-18] Cubic CaF_2 is one of the most efficient host materials for Ln luminescence, providing a low (<350 cm^{-1}) phonon energy and high viability for doping since the radius of Ca^{2+} is close to that of Ln^{3+}.[19-22] In the investigated system, the ultra-low dimensionality of the doped CaF_2 nanoparticles, achieved by employing the thermal decomposition synthetic method, is of particular importance to limit the spatial separation between the energy donor dye and the accepting dopant ion to maximize the ET efficiency.[6,26]. Density functional theory (DFT) calculations allowed for an in-depth description of the structural and electronic properties of the FITC dye upon binding to the nanoparticles, which greatly influence its optical features. We investigated the photocycle mechanism in detail by using conventional photoluminescence and advanced transient absorption (TA) spectroscopy, providing information on the luminescence dynamics both from bright (radiative) and dark (non-radiative) states. On the basis of the retrieved experimental results, the implementation of the Forster's model of resonance energy transfer and molecular modelling, we were able to shed light on the main factors which govern the dye to Er^{3+} sensitization pathway to reach exceptionally high efficiency.

2. Experimental

2.1 Synthesis

$Ca(CF_3COO)_2$ and $Ln(CF_3COO)_3$ were prepared as described in the previous research. Oleic acid (OA), oleylamine (OM), 1-octadecence (ODE), FITC were purchased from Sigma Aldrich.

Monodisperse CaF_2 were synthesized by reported thermal decomposition method.[27,29] 1 mmol $Ca(CF_3COO)_2$ was mixed with 1.6 mL of oleic acid, 1.6 mL of oleylamine, 3.2 mL of 1-octadecece in a 50 mL three-neck flask. The mixture was heated to 120 °C under nitrogen flow with vigorous stirring for 40 min, then the temperature was increased to 150 °C and retained for 30 min to form a clear yellowish solution. Afterwards, the solution was continually heated to 310 °C for 20 min, and then cooled down naturally to room temperature. The resulting solution was washed and precipitated by addition of ethanol several times, finally re-dispersed in the cyclohexane.

$CaF_2:Ln^{3+}$ was prepared in a similar manner to CaF_2, except using 0.7 mmol $Ca(CF_3COO)_2$ and 0.3 mmol $Ln(CF_3COO)_3$ reagents instead of 1 mmol $Ca(CF_3COO)_2$.

FITC functionalized CaF_2 or $CaF_2:Ln^{3+}$ nanoparticles were synthesized as follows. CaF_2 or $CaF_2:Ln^{3+}$ nanoparticles in chloroform (12 mg/mL) were mixed with FITC chloroform solution (0.3 mg/mL). The suspensions were stirring constantly for 15 h at 50 °C. The final products were washed with acetonitrile for several times, and then re-dispersed in chloroform.

2.2 Characterization

Powder X-ray diffraction (XRD) pattern was conducted on a Thermo Scientific ARL X'TRA diffractometer in the range of 20-70°. Transmission electron microscope (TEM) measurements were obtained by using a Cs-corrected JEOL JEM-2200FS TEM operated at 200 kV. The optical properties of all samples were investigated on $CHCl_3$ solutions or dispersions with a slight excess of triethylamine to ensure that the FITC dye was present in the fully deprotonated, dianionic form. The absorption spectra were performed by PerkinElmer Lambda 900 UV-Vis-NIR spectrometer. The steady-state and time-resolved photoluminescence spectra were carried out through an Edinburgh FLSP 920 UV-Vis-NIR spectrofluorometer. TA spectra were recorded by exciting suspensions of $CaF_2:Ln^{3+}$ nanoparticles using 100 femtosecond pulses at 500 nm created from an 800 nm Spitfire Ace Spectraphysics Ti:S Laser through non-linear conversion in a TOPAS optical parametric amplifier. The noise levels of 0.1 mOD (RMS) were obtained by averaging over 5000 shots per time delay. The ground-state electronic structures of FITC as free dianion and coordinated to a Ca^{2+} ion were calculated at DFT[30] level of theory using the B3LYP functionals[31,32] implemented in the GAUSSIAN 16[33] software package. The ground state geometries were acquired by full geometry optimizationmwithout any symmetry constraint both in the gas phase and $CHCl_3$ using a polarizable continuum model (PCM)[34]. The 10 lowest singlet excited states for CaF_2@FITC were calculated in $CHCl_3$ within the time dependent-DFT (TD-DFT) formalism as implemented in Gaussian.[35,36] In the case of free FITC dianion TD-DFT calculations concerned both the 20 lowest singlet and triplet excited states (50-50).The basis set employed for all atoms was the valence triple-zeta 6-311+G(d,p),[37,38] and all structures were input using ArgusLab 4.0.[39]

3. Results and discussion

The schematic energy level diagram of FITC and Er^{3+} in FITC-sensitized $CaF_2:Er^{3+}$ nanoparticles and the possible energy transfer mechanism are presented in Fig. 1. The photocycle pathway develops through multiple steps: first, photoexcitation of dye molecules populates the singlet S_1 state; subsequently, ET to the Ln^{3+} upper energy levels can happen directly from the excited singlet S_1 state (SET) or from the lower lying triplet T_1 state (TET) in turn populated through intersystem crossing (ISC) from S_1. This latter event is favoured by the strong spin orbit coupling associated to the Ln^{3+} (heavy atom effect).[24,40] Generally, energy is transferred with more efficiency to the Ln^{3+} upper levels that are close in energy to the dye donor state (resonance condition), but as a rule of thumb, the feeding state

should be higher than the acceptor emissive level to avoid energy back transfer.[23] FITC has its lowest excited singlet state at around 19000 cm^{-1}, which is suitable for Er^{3+} NIR sensitization, since the emissive level of this ion sits around 6500 cm^{-1} and is at the same time accompanied by several superior energy states that can act as accepting levels to ensure resonance with the donor states.

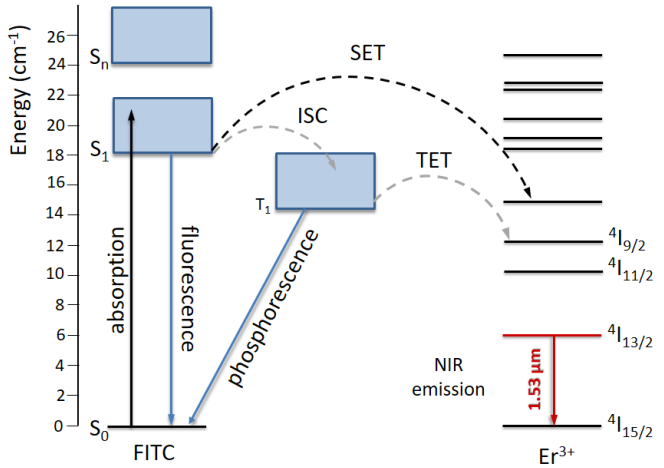

Fig. 1 The mechanism of energy transfer in the FITC sensitized Er^{3+}-doped CaF_2 nanoparticles.

CaF_2:30%Er^{3+} nanoparticles with an average size of 3.6 nm were synthesized according to a previously reported thermal decomposition method.[6] Compared to other synthetic methods, like the hydrothermal technique, the sol-gel method, and so on, the thermal decomposition method has the advantage of allowing a good control of the particle size and producing well monodispersed and crystalline nanoparticles.[27,28] A uniform distribution of spherical-like nanoparticles was obtained by taking advantage of this synthesis (Fig. 2a). The powder XRD pattern in Fig. 2b shows that the three main diffraction peaks at 28.2°, 46.9°, 55.7° are well matched with the standard cubic phase of CaF_2 (JCPDS No. 87-0971),[41] indicating that Er^{3+} doping did not significantly alter the crystal structure.

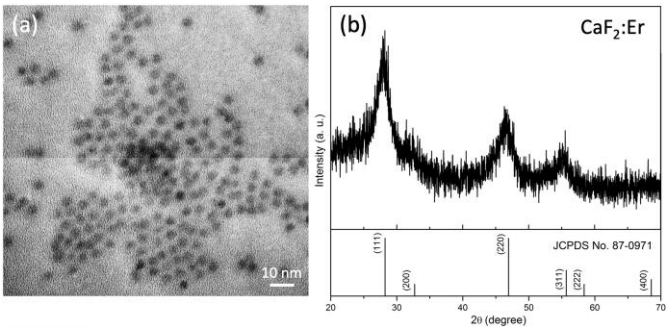

Fig. 2 (a) TEM image and (b) powder XRD pattern of CaF_2:Er^{3+} nanoparticles.

The absorption and steady-state photoluminescence spectra in the visible range of the free FITC in its dianionic form, CaF_2@FITC and CaF_2:Er^{3+}@FITC in $CHCl_3$ solution or dispersion with triethylamine as deprotonating agent (see Experimental Section), are shown in Fig. S1 and Fig. 3a, respectively. The binding interactions of FITC molecules to the surface of CaF_2 nanoparticles was confirmed by the observation of the change in the shape and intensity of the absorption spectra, as well as blue shift from 538 nm to 536 nm for the emission maximum wavelength. As shown in Fig. 3b, the luminescence decay dynamics of the free FITC and FITC-functionalized CaF_2 sample in the visible region follows a mono-exponential trend with similar time constants of 4.67 ns (R^2=0.999) and 4.28 ns (R^2=0.993), respectively. Instead, the lifetime of FITC luminescence drastically decreased down to 0.95 ns (R^2=0.991) after binding to the CaF_2:Er^{3+} nanoparticles.

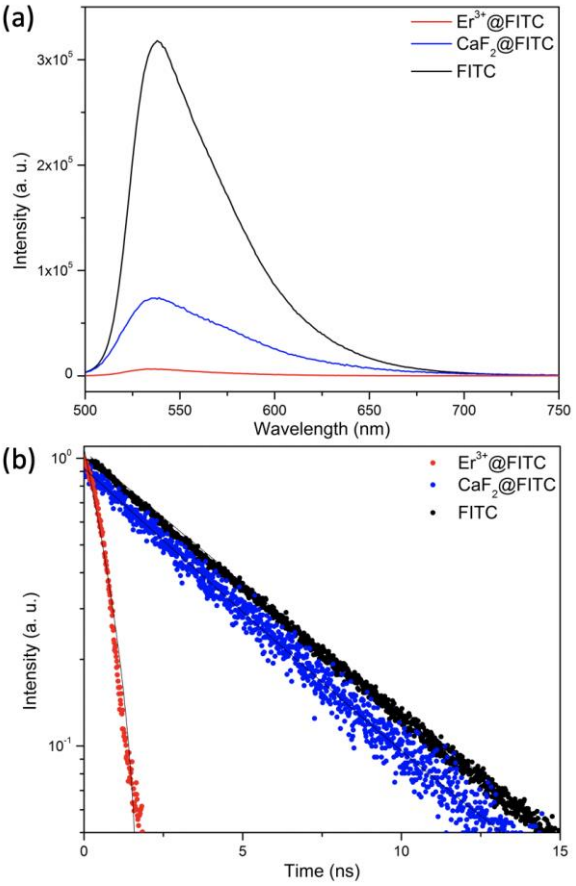

Fig. 3 (a) Vis emission spectra (λ_{ex} = 467 nm) and (b) luminescence decay curves (λ_{ex} = 467 nm; λ_{em} = 538 nm) of FITC (black), CaF_2@FITC (blue), CaF_2:Er^{3+}@FITC (red). Steady-state spectra are normalized for the absorbed power at excitation wavelength.

The change of the steady-state optical features of FITC when combined with the CaF_2 nanoparticles suggests a significant effect of the bonding on the electronic and optical properties of the dye molecule. Those phenomena can be explained by the redistribution of the electron density of the ligand upon coordination to the Ca^{2+} cation on the surface of the nanoparticle through the carboxylate group. A similar finding was verified in other types of dye-sensitized Ln^{3+}-doped nanoparticles, for instance, β-$NaYF_4$:Yb^{3+},Er^{3+}@IR-806 and with other dyes.[42, 43] To better understand this phenomenon, we performed DFT calculations to highlight the differences between the FITC dianion in the free form and when coordinated to a Ca^{2+} ion. Figures 4a and S2-3 report the DFT-

calculated optimized geometries for the two forms. As it can be seen, the FITC moiety undergoes a remarkable distortion upon coordination which leads to a significant increase of the dipole moment (from 17.41 to 24.10 Debye). The calculated molecular orbitals (MOs) for the two FITC forms, shown in Fig. 4b and Table S1, further support the previous hypothesis and highlight a redistribution of the electron cloud with more extended delocalization upon coordination of the dye moiety to the Ca^{2+} cation. Noticeably, according to time-dependent TD-DFT-calculations, the dominant optical transition for the FITC dianion in the free form (Table S2) mainly involves highly localized Highest Occupied MO (HOMO) and Lowest Unoccupied MO (LUMO) orbitals, whereas a more mixed character, involving the more delocalized LUMO+1 and LUMO+2 orbitals, is associated to the lowest energy transitions of FITC coordinated to a Ca^{2+} ion (Table S3). These findings highlight the high sensitivity of the dye dianion to the chemical environment and may account for the significant changes in the spectral shapes and intensities of both the absorption and photoluminescence spectra.

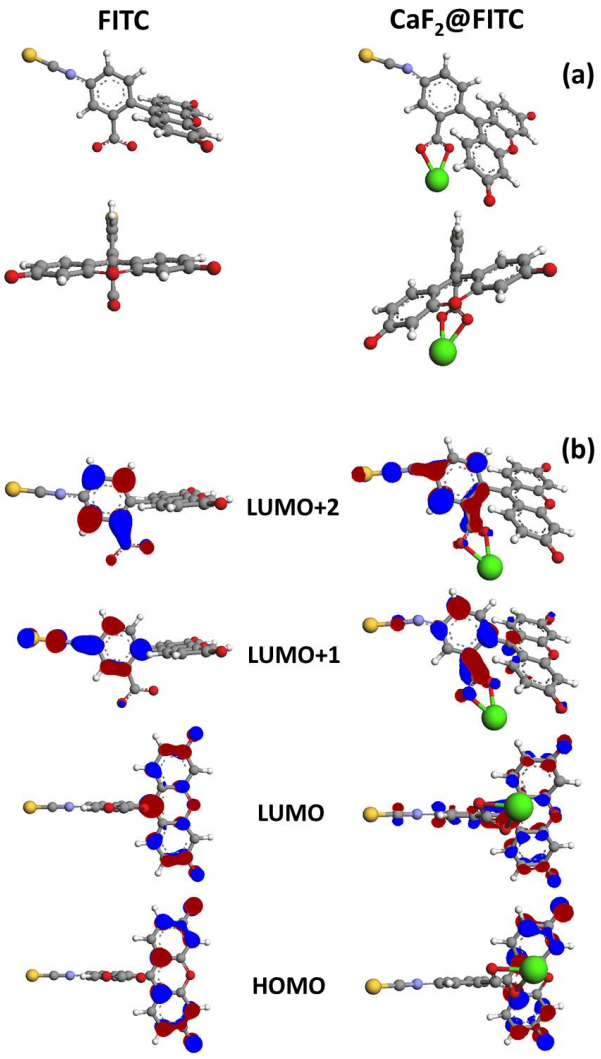

Fig. 4. Optimized geometries (a) and molecular orbitals (b) calculated by DFT methods at B3LYP/6-311+G(d,p) level of theory. The orbitals are reported with a contour value of 0.050.

On the other hand, as previously mentioned, the change of the electronic properties of the dye moiety upon coordination, while leading to a significant variation of the molecular dipole moment, does not bring to a noticeable variation of the overall oscillator strength *f* of the main transitions (tables S2-3). Under the assumption that the transition giving rise to radiative emission shares the same character of the corresponding lowest energy absorption band (implying a consistent MOs mixing for the Ca^{2+} coordinated FITC), it is not surprising that similar emission lifetimes were observed for FITC in the free form and bonded to CaF_2 nanoparticles. However, as previously mentioned, the decay dynamics becomes considerably faster as Er^{3+} ions are doped into the nanoparticles, indicating that an additional deactivation channel, likely through ET to the lanthanide ion, is established in this case. The sensitization efficiency from the donor FITC to the acceptor Ln^{3+} can be estimated by the simplified equation (1):[43]

$$\eta_{sens} = 1 - \tau_{Ln}/\tau_{dye} \quad (1)$$

where τ_{Ln} and τ_{dye} are the lifetimes of the dye in the presence and in the absence of the Ln^{3+}. Therefore, the calculated $\eta_{dye\text{-}Ln}$ is approximately 78%. The dye⟶Er^{3+} energy transfer process analysed by TA spectroscopy at the ultrafast time scale will be discussed in more details later.

The highly efficient energy transfer from FITC to Er^{3+} resulted in around 28-fold enhancement of Er^{3+} NIR emission at 1530 nm corresponding to the intrashell f-f $^4I_{13/2}\longrightarrow{}^4I_{15/2}$ transition (Fig. 5a). This provides the direct evidence that the dye⟶Er^{3+} energy transfer works well in CaF_2:Er^{3+}@FITC nanoparticles. The luminescence lifetimes at 1530 nm of CaF_2:Er^{3+} and CaF_2:Er^{3+}@FITC obtained from a double-exponential fitting (Fig. 5b), are 5750 ns (R^2=0.997) and 13414 ns (R^2=0.991), respectively. After FITC sensitization, the lifetime of Er^{3+} NIR emission increased by 2.3 times. The increase of the luminescence lifetime in the NIR could be attributed to a beneficial shielding effect of the dye to environmental vibrational quenching from solvent molecules.[44]

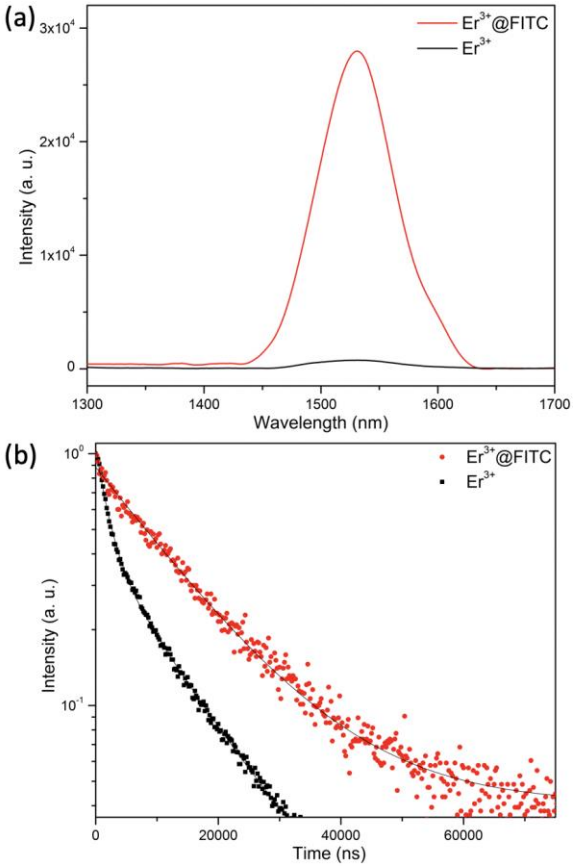

Fig. 5 (a) NIR emission spectra of $CaF_2:Er^{3+}$ (black, λ_{ex} = 378 nm) and $CaF_2:Er^{3+}$@FITC (red, λ_{ex} = 467 nm); (b) luminescence decay curves of $CaF_2:Er^{3+}$ (black, λ_{ex} = 378 nm; λ_{em} = 1530 nm) and $CaF_2:Er^{3+}$@FITC (red, λ_{ex} = 467 nm; λ_{em} = 1530 nm).

TA spectroscopy measurements have been carried out to analyse the excited state evolution of dye molecules, which can shed light on the energy transfer pathways of dye-sensitized lanthanide-doped fluoride luminescent nanoparticles. Both radiative and non-radiative channels can be unravelled from TA maps by probing the differential absorption $\Delta A = A_t - A_0$ at a delay time (t) of the probe pulse (A_t) with respect to the excitation pump at t = 0 (A_0).[45] Samples were optically pumped at 500 nm corresponding to the absorption maximum of FITC either in the free form and combined to the nanoparticles. As seen from Fig. 6a, showing the two-dimensional (2D) TA map of CaF_2@FITC as reference sample, and Fig. S4, the three samples FITC, CaF_2@FITC and $CaF_2:Er^{3+}$@FITC, all showed similar characteristic traces in the 400-750 nm range, whereas no TA signal was detected by probing in the 800-1200 nm range. The TA spectra extracted at different time delays in Fig. 6b evidence strong negative signals involving three recognizable contributions: ground-state bleaching (GSB) bands at around 475 nm and 506 nm and a stimulated emission (SE) band, appearing as a weak shoulder around 540 nm. These attributions are in agreement with the shape and position of the absorption and steady-state photoluminescence emission spectra. There is also a positive signal below 450 nm which can be attributed to excited state absorption (ESA) to upper energy levels S_n (Fig. 1). The TA spectra of the free FITC display a blue-shift (Figures S4a and S5) of the relevant features dominated by a strong negative signal in the 400-650 nm region due to GSB and SE contributions, in agreement with the absorption (Fig. S1) and photoluminescence (Fig. 3a) spectra.

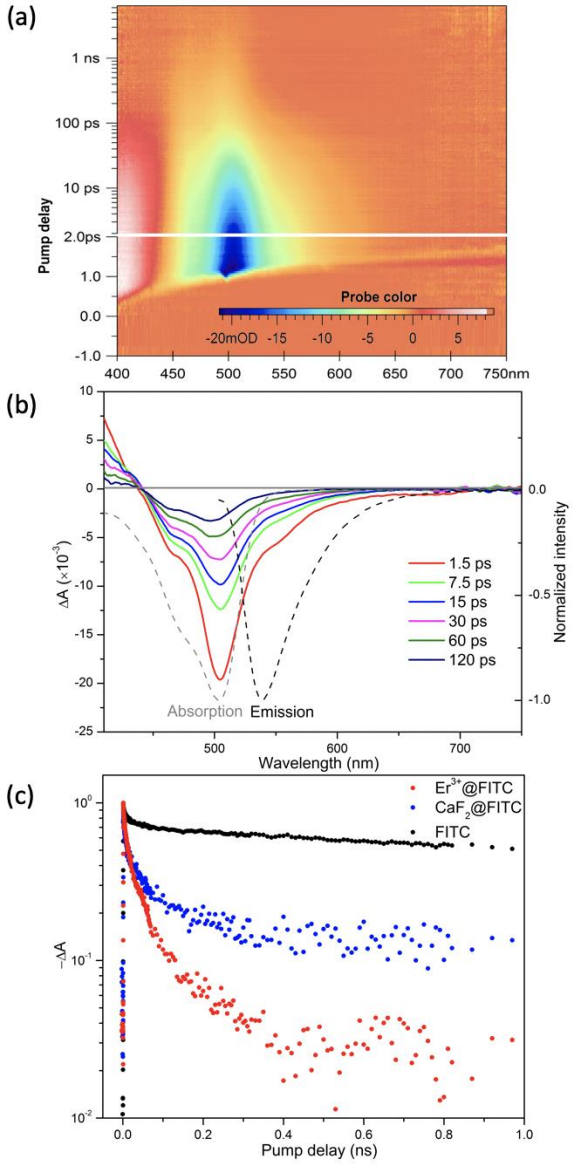

Fig. 6 (a) Two-dimensional (2D) TA (ΔA) map of $CaF_2:Er^{3+}$@FITC in chloroform as a function of wavelength and time, upon photoexcitation at 500 nm; (b) representative selection of TA spectra of $CaF_2:Er^{3+}$@FITC in chloroform at different time delays, the black and grey dash lines show the inverted PL spectrum and ground-state absorption spectrum, respectively; (c) selected kinetics of FITC, CaF_2@FITC and $CaF_2:Er^{3+}$@FITC for the SE signal at 550 nm in the sub-ns time range.

The intensity of the TA features reaches the maximum within 1 ps and subsequently decreases as the time delayed to 120 ps, with no significant changes in the spectral shape. The nearly instant signal rising in the entire probed range indicates that the TA responses of the three samples are all dominated by the excited singlet state S_1, and no signal is showing a slow and multistep activation of an excited triplet. GSB, SE and ESA show the same temporal dynamics dominating in the 100 ps range and are reliably attributed to a $S_1 \longrightarrow S_n$ (n = 0, 2, 3…) transition.

Fig. 5c displays the decay curves for the SE signal at 550 nm of all the samples as extracted from TA data.

The kinetic trace for CaF_2:Er^{3+}@FITC sample can be best fitted by a double-exponential function with a long-lived component (> 1 ns) and a short-lived component beyond the investigated temporal range (50 fs-1 ns). The relative contribution of the long-lived component to the total signal is comparable to the relative intensity of the steady-state dye luminescence emission intensity in the hybrid samples with respect to the free FITC (Fig. 3a). This component is also comparable to the time-resolved photoluminescence lifetime profiles in Fig. 3b. Interestingly, the signal for CaF_2 nanoparticles without Ln^{3+} dopants also presents a double-exponential trend with an overall signal dynamics that is faster than that of the free dye (see also Fig. S4). The emergence of the short-lived signal accompanying a longer one in the presence of the CaF_2 nanoparticles, either doped or undoped, can be attributed to the existence of distinct populations of donors interacting with the nanoparticle to a different degree. This could be modelled with a disordered arrangement of dyes consisting of FITC molecules directly and indirectly bonding to the surface of the nanoparticle due to multiple constraints related to electrostatic interactions (distribution of charges on the surface of the particle, intermolecular interactions etc…).[46] This point is highlighted by the significant change of the electron density of the Ca^{2+}-coordinated FITC with respect to the free form (Figures S6-7) which points out the high sensitivity of the system to the chemical environment. This is especially relevant when considering a poor-structurally defined system such as a collection of organic dyes interacting with a nanoparticle, which is far more complex that a simple representation of a single dye unit coordinated to a single Ca^{2+} ion. Nonetheless, in the case of CaF_2:Er^{3+}@FITC, both the short-lived and the long lived components are greatly shortened with respect to the undoped CaF_2@FITC system, indicating that energy transfer is effectively occurring from the dye to Er^{3+} at both the slow (ns range) and ultrafast (ps range) time scales. From the above considerations on the evolution of TA traces, it is also possible to conclude that the sensitization mechanism from the FITC dye to the Ln^{3+} reliably occurs through SET. In summary, the kinetic traces retrieved from TA data reveal an ultrafast energy transfer regime that remains hidden to conventional time-resolved PL experiments. This phenomenon can be related to a population of dyes that are more significantly influenced by the presence of the nanoparticle and presumably directly anchored to its surface. The retrieved time constants for the ultrafast excited singlet decay in the sub-ns region after the subtraction of the slow component are presented in Table 1, along with the calculated sensitization efficiencies. The ultrafast decay time constant of FITC coupled to CaF_2 nanoparticles is around 200 ps, and it decreases to 15 ps in the presence of Er^{3+}, showing nearly 92% sensitization efficiency. To better understand the relation between the energy transfer efficiency and the molecular arrangement in terms of the spatial separation of the donor and acceptor, we have implemented the Förster's model of resonance energy transfer on the basis of experimental data. In the model, the rate for a donor-acceptor energy transfer $\kappa_{FITC\text{-}Er}$ = $(1/\tau_{FITC\text{-}Er})$ depends on temporal, spectral and spatial parameters as described by the following equation (2):[47]

$$\kappa_{\mathrm{FITC-Er}} = \frac{1}{\tau_{\mathrm{FITC}}} \frac{9\kappa_j{}^2}{128\pi^5 n^4 R_{FITC-Er}} J = \frac{1}{\tau_{\mathrm{FITC}}} \left(\frac{R_0}{R_{FITC-Er}}\right)^6 \quad (2)$$

where $R_{FITC\text{-}Er}$ is the donor-acceptor distance; R_0 is the Förster radius, the distance at which the energy transfer efficiency reaches to 50%; τ_{FITC} is the decay time of the donor FITC in the absence of the acceptor Er^{3+}; *n* is the refractive index of the medium (taken as 1.4459 for $CHCl_3$); $\kappa_j{}^2$ is the dipole orientation factor, which is determined by the relative orientation between the transition dipole moments of the donor and the j_{th} acceptor (here 2/3 is taken for an arbitrary orientation). *J* is the spectral overlap integral between the donor FITC emission and the acceptor Er^{3+} absorption, which can be expressed by the following equation (3):[47]

$$J = \int F_{\mathrm{FITC}}(\lambda)\sigma_{\mathrm{Er}}(\lambda)\lambda^4 d\lambda \quad (3)$$

where $F_{FITC}(\lambda)$ represents the FITC emission spectral density normalized to unity (nm^{-1}), and $\sigma_{Er}(\lambda)$ is the absorption cross-section of Er^{3+} (nm^2) as shown in Fig. 7a. The calculated spectral overlap *J* and the Förster's radius R_0 are 4.8×10^3 nm^6 and 0.74 nm, respectively. On the basis of equations (1) and (2), the dependence of the sensitization efficiency from the donor-acceptor distance R can be predicted as shown by the plot in Fig. 7b. As seen from Fig. 7b, the curve presents a plateau at values almost close to unity as the donor-acceptor distance is below ~0.4 nm, and it drops dramatically when the distance is beyond this range. The experimental sensitization efficiency around 92% retrieved from the TA kinetic data shown in Table 1 corresponds to donor-acceptor distances in the range 0.45-0.50 nm. These values are compatible with the spatial separation of the DFT-calculated transition dipole moment vector for the optimized geometry upon bonding of the FITC molecules, as depicted in the inset of Fig. 7b. Therefore, the exceptional dye-to-Er^{3+} sensitization efficiency at the ultrafast time scale in the CaF_2:Er^{3+}@FITC nanoparticles is consistent with the small size and the particular geometrical construction of FITC molecules attached to the surface of the CaF_2:Er^{3+} nanoparticle. Instead, the "slow" energy transfer occurring at the nanosecond time scale could be associated with dye molecules that are not optimally arranged on the surface of the particle (not directly bonded or distorted). These results highlight that small variations of the donor-acceptor distances in the sub-nanometre range can dramatically affect the sensitization efficiency in dye-sensitized erbium-doped nanoparticles.

Table 1. FITC excited singlet ultrafast decay time constants and FITC to Er^{3+} sensitization efficiency calculated through Eq. (1).

Sample	τ (ps)	η_{sens} (%)
FITC	∞	-
CaF_2	200 (10)	-
Er^{3+}	15 (2)	92

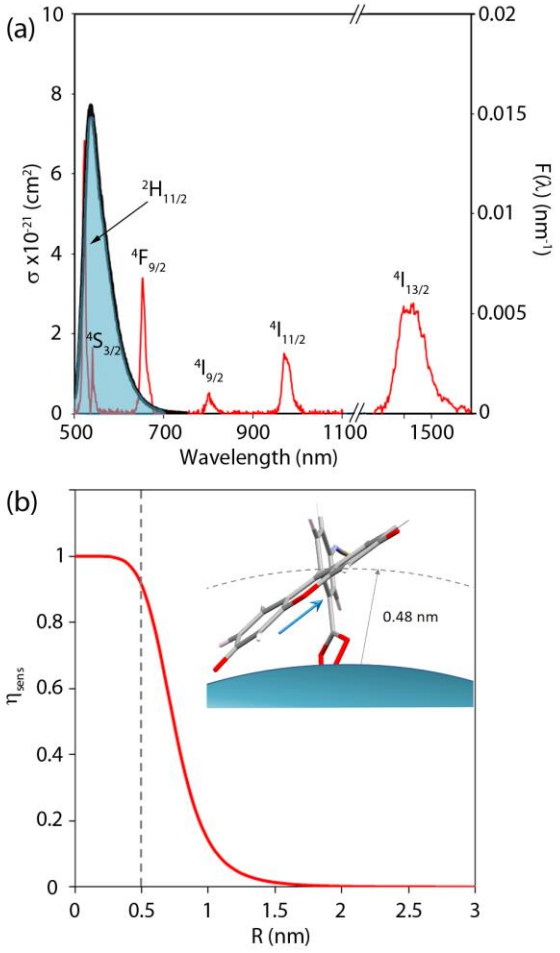

Fig. 7 (a) Spectral overlap of Er^{3+} absorption cross-section (red) and FITC fluorescence spectrum normalized to unity (black curve with shaded area). **(b).** FITC to Er^{3+} sensitization efficiency (η_{sens}) calculated by the Förster's model as a function of the donor-acceptor distance (R). Inset: DFT-calculated optimized geometry for FITC coordinated to Ca^{2+} where the light blue arrow represents the TD-DFT calculated S_1-S_0 transition dipole moment.

Conclusions

In conclusion, we have provided the first in-depth study of the structural, electronic and photophysical properties of dye-sensitized Er^{3+} nanoparticles and highlighted the key factors that regulate the emission efficiency in the NIR. We have shown that the FITC dye molecules undergo significant changes of the structure and electronic distribution when binding to a nanoparticle, which dramatically influence their optical properties. By a unique combination of conventional photoluminescence and transient absorption spectroscopy, we were able to unravel the detailed mechanism of energy transfer at the organic-inorganic interface. Sensitization occurs directly through the dye singlet state in different time regimes, at the nanosecond and at the picosecond time-scale indicating that different populations of dyes, differently arranged around the nanoparticle, contribute to the energy transfer process. The combination of a rational design of the nanoparticle, whose dimensionality is kept below 3.6 nm and the distortion of the FITC moiety, which implies a sub-0.5 nm spatial separation of its transition dipole moment from the surface of the nanoparticle, leads to a distance between the energy donors (FITC dyes) and acceptors (Er^{3+} ions) well below the Förster's radius (0.74 nm). This results in an exceptional sensitization efficiency of the FITC dye to Er^{3+} reaching up to 92% and a 28-fold increase of the emission intensity at 1530 nm with respect to bare doped nanoparticles.

These results highlight that, to achieve highly efficient energy transfer in dye-sensitized lanthanide-doped nanoparticles, dye molecules must be reasonably designed so that they have suitable excited singlet energy states and localized molecular orbitals (transition dipole moments) close to the surface of the nanoparticle. This proof of concept of dye-sensitized Er^{3+} NIR emission can promote new opportunities for a superior improvement of optical fiber amplifiers and other photonic technologies working at 1.5 µm.

Conflicts of interest

There are no conflicts to declare.

Acknowledgements

This work was supported by National Natural Science Foundation of China (NSFC) (Grant No. 52002336), Fundamental Research Funds for the Central Universities (SWU019041), and the Science and Technology project of Chongqing Education Committee (No. KJCX2020005), Chongqing Engineering Research Center for Rapid Diagnosis of Dread Disease and Chongqing Engineering Research Center for Micro-Nano Biomedical Materials and Devices, Southwest University, China (JL). This project has also received funding from the FWO and European Union's Horizon 2020 research and innovation program under the Marie Skodowska-Curie grant agreement No.665501 (12U3417N LV) (FA).

Notes and references

1 J. Liu, A. M. Kaczmarek and R. Van Deun, *Chem. Soc. Rev.*, 2018, **47**, 7225-7238.
2 J.-C. G. Bünzli and C. Piguet, *Chem. Soc. Rev.*, 2005, **34**, 1048-1077.
3 F. Artizzu, F. Quochi, L. Marchiò, C. Figus, D. Loche, M. Atzori, V. Sarritzu, A. M. Kaczmarek, R. Van Dun, M. Saba, A. Serpe, A. Mura, M. L. Mercuri, G. Bongiovanni and P. Deplano, *Chem. Mater.*, 2015, **27**, 4082-4092.
4 K. Kuriki, Y. Koike and Y. Okamoto, *Chem. Rev.*, 2002, 102, **6**, 2347-2356.
5 D. Tu, L. Liu, Q. Ju, Y. Liu, H. Zhu, R. Li and X. Chen, *Angew. Chem. Int. Edit.*, 2011, **50**, 6306-6310.
6 J. Liu, A. M. Kaczmarek, F. Artizzu and R. Van Deun, *ACS Photonics*, 2019, **6**, 659-666.

7 W. G. Van Sark, J. De Wild, J. K. Rath, A. Meijerink and R. EI Schropp, *Nanoscale Res. Lett.*, 2013, **8**, 81.

8 J.-C. G. Bünzli and A.-S. Chauvin, in *Handbook on the Physics and Chemistry of Rare Earths*, ed. J.-C. G. Bünzli and V. K. Pecharsky, Elsevier North Holland, Amsterdam, 2014, vol. 44, pp. 169-281.

9 T. Kitagawa, K. Hattori, K. Shuto, M. Yasu, M. Kobayashi and M. Horiguchi, *Electron. Lett.*, 1992, **28**, 1818-1819.

10 Y. C. Yan, A. J. Faber, H. De Waal, A. P. Polman and G. Kik, *Appl. Phys. Lett.*, 1997, **71**, 2922-2924.

11 W. You, Y. Huang, Y. Chen, Y. Lin and Z. Luo, *Opt. Commun.*, 2008, **281**, 4936-4939.

12 J. Zhou and D. Jin, *Nat. Photonics*, 2018, **12**, 378-379.

13 X. Wang, R. R. Valiev, T. Y. Ohulchanskyy, H. Ågren, C. Yang and G. Chen, *Chem. Soc. Rev.*, 2017, **46**, 4150-4167.

14 Q. Liu, X. Zou, Y. Shi, B. Shen, C. Cao, S. Cheng, W. Feng and F. Li, *Nanoscale*, 2018, **10**, 12573-12581.

15 L. Yuan, W. Lin, K. Zheng, L. He and W. Huang, *Chem. Soc. Rev.*, 2013, **42**, 622-661.

16 T. Y. Lin, Z. J. Lian, C. X. Yao, X. Y. Sun, X. Y. Liu, Z. Y. Yan and S. M. Wu, *RSC Adv.*, 2020, **10**, 260-270.

17 L. W. Runnels and S. F. Scarlata, *Biophys. J.*, 1995, **69**, 1569-1583.

18 R. G. McClelland and A. C. Pinder, *Appl. Environ. Microbiol.*, 1994, **60**, 4255-4262.

19 P. Huang, W. Zheng, S. Zhou, D. Tu, Z. Chen, H. Zhu, R. Li, E. Ma, M. Huang and X. Chen, *Angew. Chem. Int. Ed.*, 2014, **53**, 1252-1257.

20 Z. Li, Y, Zhang, L. Huang, Y. Yang, Y. Zhao, G. El-Banna and G. Han, *Theranostics*, 2016, **6**, 2380-2393.

21 B. Xu, D. Li, Z. Huang, C. Tang, W. Mo and Y. Ma, *Dalton Trans.*, 2018, **47**, 7534-7540.

22 W. Yin, G. Tian, W. Ren, L. Yan, S. Jin, Z. Gu, L. Zhou, J. Li and Y. Zhao, *Dalton Trans.*, 2014, **43**, 3861-3870.

23 B. Xue, D. Wang, L. Tu, D. Sun, P. Jing, Y. Chang, Y. Zhang, X. Liu, J. Zuo, J. Song, J. Qu, E. J. Meijer, H. Zhang and X. Kong, *J. Phys. Chem. Lett.*, 2018, **9**, 4625-4631.

24 D. J. Garfield, N. J. Borys, S. M. Hamed, N. A. Torquato, C. A. Tajon, B. Tian, B. Shevitski, E. S. Barnard, Y. D. Suh and S. Aloni, *Nat. Photonics*, 2018, **12**, 402-407.

25 Z. Wang and A. Meijerink, *J. Phys. Chem. Lett.*, 2018, **9**, 1522-1526.

26 S. Wen, J. Zhou, P. J. Schuck, Y. D. Suh, T. W. Schmidt and D. Jin, *Nat. Photonics*, 2019, **13**, 828-838.

27 J. C. Boyer, F. Vetrone, L. A. Cuccia and J. A. Capobianco, *J. Am. Chem. Soc.*, 2016, **128**, 7444-7445.

28 M. He, P. Huang, C. Zhang, F. Chen, C. Wang, J. Ma, R. He and D. Cui, *Chem. Commun.*, 2011, **47**, 9510-9512.

29 B. Xu, H. He, Z. Gu, S. Jin, Y. Ma and T. Zhai, *J. Phys. Chem. C*, 2017, **121**, 18280-18287.

30 R. G. Parr and W. Yang, Density functional theory of atoms and molecules, 1989, Oxford University Press, Oxford.

31 D. Becke, *J. Chem. Phys.*, 1993, **98**, 5648-5652.

32 C. Lee, W. Yang and R. G. Parr, *Phys. Rev. B*, 1988, **37**, 785-789.

33 M. J. Frisch, G. W. Trucks, H. B. Schlegel, G. E. Scuseria, M. A. Robb, J. R. Cheeseman, G. Scalmani, V. Barone, G. A. Petersson, H. Nakatsuji, X. Li, M. Caricato, A. V. Marenich, J. Bloino, B. G. Janesko, R. Gomperts, B. Mennucci, H. P. Hratchian, J. V. Ortiz, A. F. Izmaylov, J. L. Sonnenberg, D. Williams-Young, F. Ding, F. Lipparini, F. Egidi, J. Goings, B. Peng, A. Petrone, T. Henderson, D. Ranasinghe, V. G. Zakrzewski, J. Gao, N. Rega, G. Zheng, W. Liang, M. Hada, M. Ehara, K. Toyota, R. Fukuda, J. Hasegawa, M. Ishida, T. Nakajima, Y. Honda, O. Kitao, H. Nakai, T. Vreven, K. Throssell, J. A. J. Montgomery, J. E. Peralta, F. Ogliaro, M. J. Bearpark, J. J. Heyd, E. N. Brothers, K. N. Kudin, V. N. Staroverov, T. A. Keith, R. Kobayashi, J. Normand, K. Raghavachari, A. P. Rendell, J. C. Burant, S. S. Iyengar, J. Tomasi, M. Cossi, J. M. Millam, M. Klene, C. Adamo, R. Cammi, J. W. Ochterski, R. L. Martin, K. Morokuma, O. Farkas, J. B. Foresman and D. J. Fox, *Gaussian, Inc., Wallingford, CT*, 2016.

34 M. Cossi, N. Rega, G. Scalmani and V. Barone, *J. Comp. Chem.*, 2003, **24**, 669-681.

35 M. E. Casida, C. Jamorski, K. C. Casida, D. R. Salahub, *J. Chem. Phys.* 1998, **108**, 4439-4449.

36 R. E. Stratmann, G. E. Scuseria, M. J. Frisch, *J. Chem. Phys.* 1998, **109**, 8218-8224.

37 A. D. McLean and G. S. Chandler, *J. Chem. Phys.*, 1980, **72**, 5639-5648.

38 R. Krishnan, J. S. Binkley, R. Seeger and J. A. Pople, *J. Chem. Phys.*, 1980, **72**, 650-654.

39 M. A. Thompson, ArgusLab 4.0.1, Planaria Software LLC: Seattle, WA, 2004. Available at: http://www.arguslab.com/arguslab.com/ArgusLab.html/.

40 C. Du, H. Wang, F. Yang and P. C. Hammel, *Phys. Rev. B*, 2014, **90**, 140407(R).

41 M. Verziu, M. Serano, B. Jurca, V. I. Parvulescu, S. M. Coman, G. Scholz and E. Kemnitz, *Catal. Today*, 2018, **306**, 102-110.

42 W. Zou, C. Visser, J. A. Maduro, M. S. Pshenichnikov and J. C. Hummelen, *Nat. Photonics*, 2012, **6**, 560-564.

43 W. Shao, C. K. Lim, Q. Li, M. T. Swihart and P. N. Prasad, *Nano Lett.*, 2018, **18**, 4922-4926.

44 P. Geiregat, J. Maes, K. Chen, E. Drijvers, J. De Roo, J. M. Hodgkiss and Z. Hens, *ACS Nano*, 2018, **12**, 10178-10188.

45 W. R. Browne and J. G. Vos, *Coord. Chem. Rev.*, 2001, 761-787.

46 J. Liu, P. Geiregat, L. Pilia, R. Van Deun and F. Artizzu, *Adv. Opt. Mater.*, 2021, 2001678.

47 T. Förster, *Discuss. Faraday Soc.*, 1959, **27**, 7-17.